Electronic Supplementary Information

Ultra-large dipole moment organic cation derived 3D/2D p-n heterojunction for high-efficiency carbon-based perovskite solar cells

Yu Lin,[a] Jiawei Tang,[a] Haocong Yan,[a] Jiaru Lin,[a] Wenran Wang,[a] Shengsen Zhang,[a] Huashang Rao,[a] Zhenxiao Pan,*[a] and Xinhua Zhong*[a]

[a]Key Laboratory for Biobased Materials and Energy of Ministry of Education, College of Materials and Energy, South China Agricultural University, Guangzhou 510642, China

E-mail: zxpan@scau.edu.cn; zhongxh@scau.edu.cn.

Experimental Section

Chemicals

Materials used in experiments include cesium iodide (CsI, 99.999%, Alfa Aesar), formamidine acetate (FAAc, 99%, Alfa Aesar), *N*,*N*-dimethylformamide (DMF, 99.8%, Sigma Aldrich), 2-propanol (IPA, 99.5%, Sigma Aldrich), lead chloride ($PbCl_2$, 99.99%, Aladdin), 1-methyl-2-pyrrolidone (NMP, 99.5%, Alfa Aesar), oleyamine (OAm, 80-90%, Acros), lead iodide (PbI_2, 99.99%, Xi'an Polymer Light Technology Co., Ltd.), hydroiodic acid (HI, 55%-58%, Aladdin), tin chloride dihydrate ($SnCl_2{\cdot}2H_2O$, 99.995%, Sigma Aldrich), urea (99%, Macklin), thioglycolic acid (TGA, 99%, Sigma Aldrich), hydrochloric acid (HCl, 36%, Guangzhou Chemical Reagent), carbon paste (DD-10, Saidi). All the chemicals were used without further purification.

Synthesis of oleylammoniun iodide

12.5 mL of oleyamine and 100 mL of anhydrous ethanol were stirred in a round-bottom flask at 0 ^{o}C. Then 10 mL of HI was added dropwise into the mixed solution, which was kept stirring overnight in nitrogen at room temperature. OLAI was obtained after evaporating the solvent. The product was recrystallized with the use of diethyl ether three times to obtain a white or yellowish solid.[1]

Synthesis of formamidine iodide

50 g of FAAc and 75 mL of HI were stirred in a round-bottom flask at 60 ^{o}C for 2.0 h. FAI crystals were obtained after evaporating the solvent and recrystallizing with diethyl ether.

Preparation of SnO_2 electron transport layer

F-doped SnO_2 (FTO) glasses were first cleaned with detergent, deionized water, ethanol, acetone, and ethanol in sequence. SnO_2 electron transport layer was constructed through a chemical bath deposition (CBD) technique. 5.0 g of urea, 100 uL of TGA, 5.0 mL of HCl were dissolved in 400 mL of ultrapure water at 0 ^{o}C. 1.096 g $SnCl_2{\cdot}2H_2O$ was dissolved in the solution and stored in a fridge. Before CBD, the Sn^{2+} precursor solution was diluted by 6 times with ultrapure water, in which the FTO glass was soaked at 80 ^{o}C for 3.0 h. After the CBD process, the glass was cleaned with ultrapure water and annealed at 180 ^{o}C for 1h.[2] Prior to the deposition of perovskites, the compact SnO_2 substrates were treated with UV-ozone for 15 min.

Fabrication process of $FA_{0.83}Cs_{0.17}PbI_3$ perovskite films

The perovskite precursor solution was prepared by dissolving 100 μL of NMP, 0.1428 g of FAI, 0.0442 g of CsI, 0.0278 g of $PbCl_2$, and 0.461 g of PbI_2 in 500 μL of DMF. The precursor solution was spin-coated on SnO_2 substrates at 2000 rpm for 15 s and then at 3000 rpm for 10 s. The air flow was introduced from a compressed air gun at the 10th second of the spin-coating process, and the perovskite films were quenched for 5 s. After the spin-coating process, the obtained perovskite films were annealed at 70 ^{o}C for 5 min in the air glove box, and then annealed at 150 ^{o}C for 17 min in ambient conditions in an isolation room with temperature and humidity control by the air conditioner and dehumidifier/humidifier (25 ± 2 ^{o}C, RH = 50 ± 5%).

Fabrication of 3D/2D perovskite layer

The OLAI precursor solution in IPA was deposited on the perovskite layer through a dynamic spin-coating method in a dry air environment, where the solution was dipped onto the spinning film dropwise slowly at 4000 rpm. Then, the films were annealed on a hot plate at 100 ^{o}C for 10 min.

Preparation of carbon electrode

Carbon paste was painted onto the perovskite layer by doctor blading and then annealed at 120 ^{o}C for 10 min in ambient with relative humidity of ~ 30%.

Preparation of pure $OLA_2FAPb_2I_7$ and $BA_2FAPb_2I_7$ 2D perovskite films

A saturated $OLA_2FAPb_2I_7$ stoichiometric perovskite solution was prepared in DMF at 70 ^{o}C. The solution underwent a slow temperature decrease (less than 10 ^{o}C per hour), and red 2D perovskite crystals were obtained at 28 ^{o}C. After the separation and drying process, the red 2D perovskite crystals were dissolved in DMF solution and spin-coated on FTO to obtain the pure 2D perovskite films for XRD and UPS tests. The $BA_2FAPb_2I_7$ films were prepared by a similar method.

Preparation of pure $PEA_2FAPb_2I_7$ 2D perovskite film

Firstly, an ultra-thin 3D perovskite layer with a thickness of about 100 nm was prepared with a high spin-coating speed (more than 8000 rpm). Then, a PEAI-FAI IPA solution with a molar ratio of 2:1 was spin-coated on the surface to convert the 3D perovskite into pure $PEA_2FAPb_2I_7$ 2D perovskite.[3]

Characterization

J–V curves of PSCs were measured by Keithley 2401 source meter equipped with a 300 W AM 1.5 G solar simulator (ORIEL-SOL3A 94023A). Calibration was taken by an NREL standard Si solar cell to set

the power of the simulated solar light to 100 mW cm^{-2}. During the measurement, the photoactive area was defined by a shading mask (0.125 cm^2). The light intensity-dependent *J–V* measurements employed neutral-density optical filters to modulate light intensity. The stabilized power output (SPO) was measured at the maximum power point with a constant voltage (0.853 V for the 3D device and 0.926 V for the 3D/2D-O device) using a xenon lamp light source. The UV-visible absorption and photoluminescence (PL) emission spectra were recorded from a UV-visible spectrophotometer (Shimadzu UV-2600) and an optical fiber fluorescence spectrophotometer (Ocean Optics, halogen lamp), respectively. The morphology and device structure of perovskite film was characterized by a field-emission scanning electron microscope (Pharos, Phenom). XRD spectra were measured on an X-ray powder diffractometer (MINIFLEX600, RIGAKU) with Cu K_α (0.15405 nm) irradiation at 36 kV and 30 mA. Grazing incidence wide-angle X-ray scattering (GIWAXS) was conducted on Taiwan light source beamlines TLS BL13A1. A round CCD detector with 165 mm diameter was used to collect the two-dimensional X-ray scattering and diffraction patterns with available q range from 0.05 $Å^{-1}$ to 2.5 $Å^{-1}$. The samples were measured at a wavelength of 1.02710 Å and STD of 229 mm. External quantum efficiency (EQE) tests were measured using a Keithley 2000 multimeter with the illumination of a 300 W tungsten lamp with a Spectral Product DK240 monochromator. Electrochemical impedance spectroscopy (EIS) was carried out on an electrochemical workstation (Zahner, Zennium) under dark conditions at forward bias voltages of 1.05 V by applying a 10 mV AC sinusoidal signal with the frequency ranging from 1 MHz to 1 Hz. For TPV/TPC measurements, the devices were illuminated by a white light-emitting diode (30 W), a small perturbation was generated by an attenuated laser pulse (532 nm, 1.344 ns), and the data were monitored by an oscilloscope (RIGOL, DS2302A). Time-resolved photoluminescence (TRPL) measurements were carried out by Edinburgh Instruments (Edinburgh, U.K.) FSL1000 spectrofluorometer equipped with a 450 nm laser as the light source. For the SCLC tests, the electron-only devices with the structure of FTO/SnO_2/perovskite/PCBM/Ag were fabricated. Then, the devices were placed in a dark vacuum device for *J–V* testing. Ultraviolet photoelectron spectra (UPS) were obtained from X-ray photoelectron spectroscopy/ESCA (ESCALAB Xi+, Thermo Fisher Scientific). Kelvin probe force microscopy (KPFM) spectra were obtained from an atomic force microscope (Dimension Icon, BRUKER). The contact angle was measured by a Krüss drop-shape analyzer (DSA25E). The Pb leakage test was carried out following the literature method.[4] The perovskite films with or without OLAI treatment were fabricated on FTO glasses and soaked in 20 mL ultra-pure water in a glass vial for different time. Then, the Pb concentrations were tested by ICP-MS (7700, Agilent technologies). The water tolerance tests of C-PSCs were carried out by soaking the devices directly in ultra-pure water and taking them out every 30 s to test the PCE for each device. Before testing, the devices were wiped by tissue and then tested directly without drying thoroughly. The maximum power point

(MPP) tracking tests were performed on a multi-channel solar cell stability test system (Wuhan 91PVKSolar Technology Co. Ltd, China).

Note S1: Calculation of energy levels of 3D and 2D perovskite.

Cutoff energies ($E_{cutoff,1}$ and $E_{cutoff,2}$) are extracted from UPS spectra at high and low binding energy regions, respectively. It is particularly important to note that the intensity needs to be converted to the logarithmic scale to avoid overestimating of the valence band edge from UPS measurements.[5] The Fermi level of the instrument has been calibrated by ultrapure Ag sample, and the work function Φ of the samples can be calculated by Equation 1:

$$E_F = \Phi = 21.22 - E_{cutoff,1} \quad (1)$$

where 21.22 eV is the photon energy of the light source (He I radiation), and Φ corresponds to the Fermi level (E_F) of the sample. Then, the valence band maximum (E_{VB}) is calculated by the energy difference between E_F and hole transport barrier ($E_{cutoff,2}$):

$$E_{VB} = E_F - E_{cutoff,2} \quad (2)$$

Finally, the conduction band minimum (E_{CB}) was calculated according to the band gap (E_g) of the sample:

$$E_{CB} = E_{VB} + E_g \quad (3)$$

where E_g is determined from the Tauc plot. Tauc plot is transformed based on UV-visible diffuse reflectance spectra according to the Tauc equation:

$$(\alpha h\nu)^{1/n} = A(h\nu - E_g) \quad (4)$$

where α is the absorption coefficient, $h\nu$ is the photon energy, A is a constant known as the band tailing parameter, n is the power factor of the transition mode. For perovskite (direct gap semiconductor), n = 0.5. Among them,

$$h\nu = 1240/\lambda \quad (5)$$

where λ is the wavelength. For the fixed perovskite layer thickness, $A(\lambda) \propto \alpha(\lambda)$, so $Ah\nu$ is reasonably applied as the vertical axis instead of $\alpha h\nu$, and E_g is derived from the intercept of the horizontal $h\nu$ axis by extrapolating a straight line in the Tauc plot.

Note S2: Work function calculation principle of KPFM.

The premise is that the work function of the probe remains constant, and the work functions of Au or highly oriented pyrolytic graphite (HOPG) are relatively stable and known. Au (WF = 5.1eV) or HOPG (WF = 4.6 eV) is usually used as a calibration sample. Then, the WF of the probe can be calculated by using this probe to test the contact potential difference (CPD) between the probe and the Au or HOPG sample.

The WF of the probe is related to the conditions under which the bias voltage is applied to the probe or sample during the KPFM tests.

If the bias voltage is applied to the probe:

$$\text{CPD} = \text{potential of the sample } (_{sample}) - \text{potential of the probe } (_{probe})$$

If a bias voltage is applied to the sample:

$$CPD = {}_{probe} - {}_{sample}$$

In this work, a bias voltage is applied to a Tap150E-G probe, and the calibration standard is freshly peeled highly oriented pyrolytic graphite (HOPG). WF of the probe can be calculated by the following equation:

$$CPD = {}_{HOPG} - {}_{probe} = (WF_{HOPG} - WF_{probe})/-e$$

After obtaining the WF value of the probe, the sample can be tested with the probe. Taking the 3D perovskite sample as an example:

$$CPD = {}_{3D} - {}_{probe} = (WF_{3D} - WF_{probe})/-e$$

The WF of the sample can be calculated based on the CPD and the WF value of the probe.

Note S3: The analysis of the efficiency loss by the Shockley-Queisser (S-Q) model.

The band gap of the perovskite used in this work is 1.55 eV. The parameters of the Shockley-Queisser (S-Q) limit in the table were calculated via a publicly available Python-based script (https://github.com/marcus-cmc/Shockley-Queisser-limit?tab=readme-ov-file).[6]

According to the S-Q model, the actual total power conversion efficiency loss of the device can be expressed as PCE/PCE^{SQ}. The V_{oc}, J_{sc}, and FF corresponding to the real PCE and S-Q limit PCE can be split into five items to express five different loss pathways, respectively, as described by the following equation:

$$\frac{PCE}{PCE^{SQ}} = \frac{J_{sc}V_{oc}^{real}FF^{real}}{J_{sc}^{SQ}V_{oc}^{SQ}FF_0(V_{oc}^{SQ})} = \frac{J_{sc}V_{oc}^{real}V_{oc}^{rad}FF_0(V_{oc}^{real})FF^{real}}{J_{sc}^{SQ}V_{oc}^{rad}V_{oc}^{SQ}FF_0(V_{oc}^{SQ})FF_0(V_{oc}^{real})}$$

Among them, the J_{sc}/J_{sc}^{SQ} corresponds to photocurrent loss, $V_{oc}^{real}/V_{oc}^{rad}$ corresponds to V_{oc} loss owing to the non-radiative recombination, V_{oc}^{rad}/V_{oc}^{SQ} corresponds to V_{oc} loss due to the discrepancy between the actual absorption coefficient and the assumed step function in the S-Q limit, $FF_0(V_{oc}^{real})/FF_0(V_{oc}^{SQ})$ corresponds to FF loss due to the loss in V_{oc}, $FF^{real}/FF_0(V_{oc}^{real})$ corresponds to FF loss due to the resistive and ideality factor.[7-9]

V_{oc}^{rad} is the radiative limit of the V_{oc} and the difference between it and the real V_{oc} of the device (V_{oc}^{real}) is non-radiative open-circuit voltage loss (ΔV_{oc}^{nrad}), calculated by the following equation:

$$V_{oc}^{rad} - V_{oc}^{real} = \Delta V_{oc}^{nrad} = -\frac{kT}{q} ln(Q_e^{lum})$$

Q_e^{lum} is the external luminescence quantum efficiency.

$FF_0(V_{oc})$ represents the FF corresponding to V_{oc} without resistive losses, calculated by the following equation:

$$FF_0 = \frac{\frac{qV_{oc}}{n_{id}kT} - ln\frac{qV_{oc}}{n_{id}kT} + 0.72}{\frac{qV_{oc}}{n_{id}kT} + 1}$$

q is the elementary charge, k is the Boltzmann constant, and T is the temperature. The ideality factor of $n_{id} = 1$ was assumed.

Computational Methods

All the calculations are performed in the framework of the density functional theory with the projector augmented plane-wave method, as implemented in the Vienna ab initio simulation package.[10] The generalized gradient approximation proposed by Perdew-Burke-Ernzerhof (PBE) is selected for the exchange-correlation potential.[11] The cut-off energy for plane wave is set to 500 eV. The energy criterion is set to 10^{-5} eV in iterative solution of the Kohn-Sham equation. All the structures are relaxed until the residual forces on the atoms have declined to less than 0.02 eV/Å. To avoid interlaminar interactions, a vacuum spacing of 18 Å is applied perpendicular to the slab. The Heyd-Scuseria-Ernzerhof (HSE06) hybrid functional was chosen for a more reliable calculation of electronic properties to avoid the PBE functional's underestimating the bandgap of the semiconductor.[12]

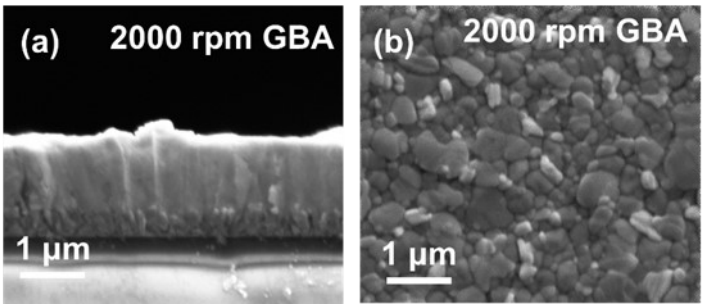

Fig. S1 (a) Cross-section and (b) top-view SEM images of perovskite films.

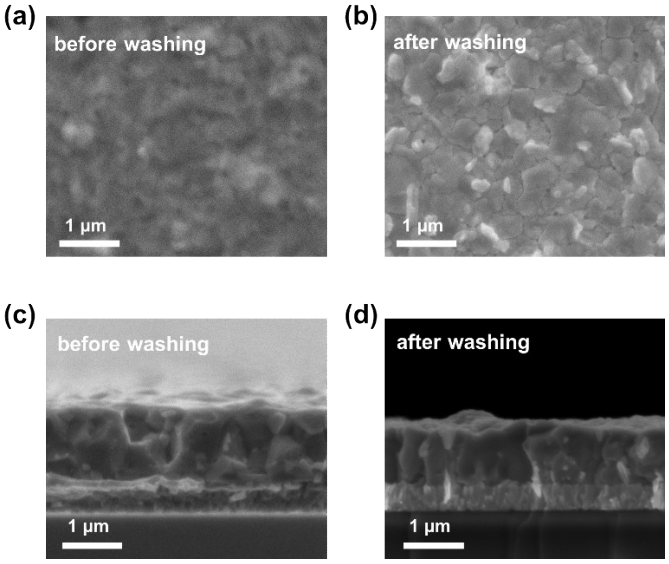

Fig. S2 The top-view and cross-sectional SEM images of the 3D/2D heterojunction film before (a,c) and after (b,d) IPA washing.

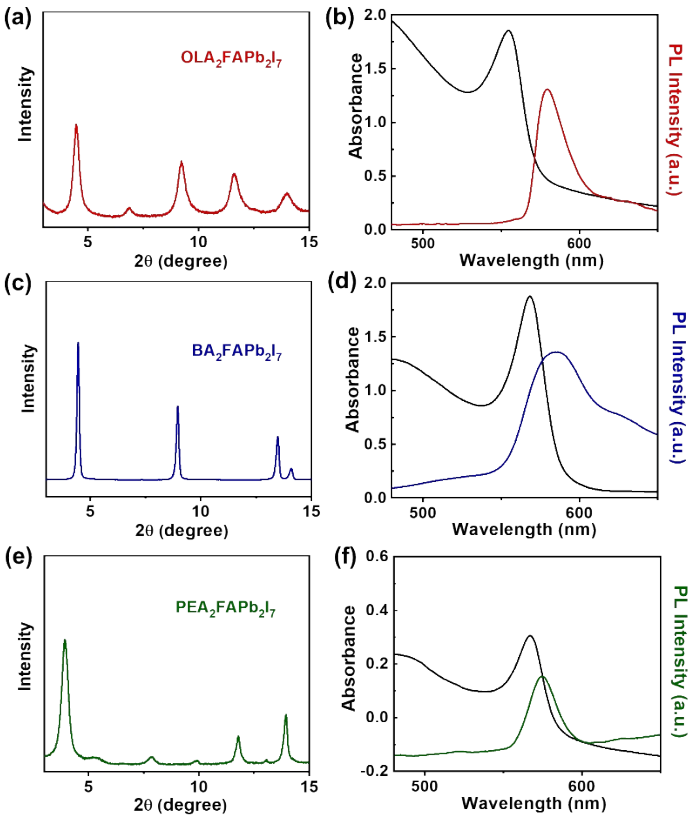

Fig. S3 (a,c,e) XRD pattern, (b,d,f) UV-vis absorbance and PL spectra of $OLA_2Pb_2I_7$, $BA_2FAPb_2I_7$, and $PEA_2FAPb_2I_7$ perovskite films, respectively.

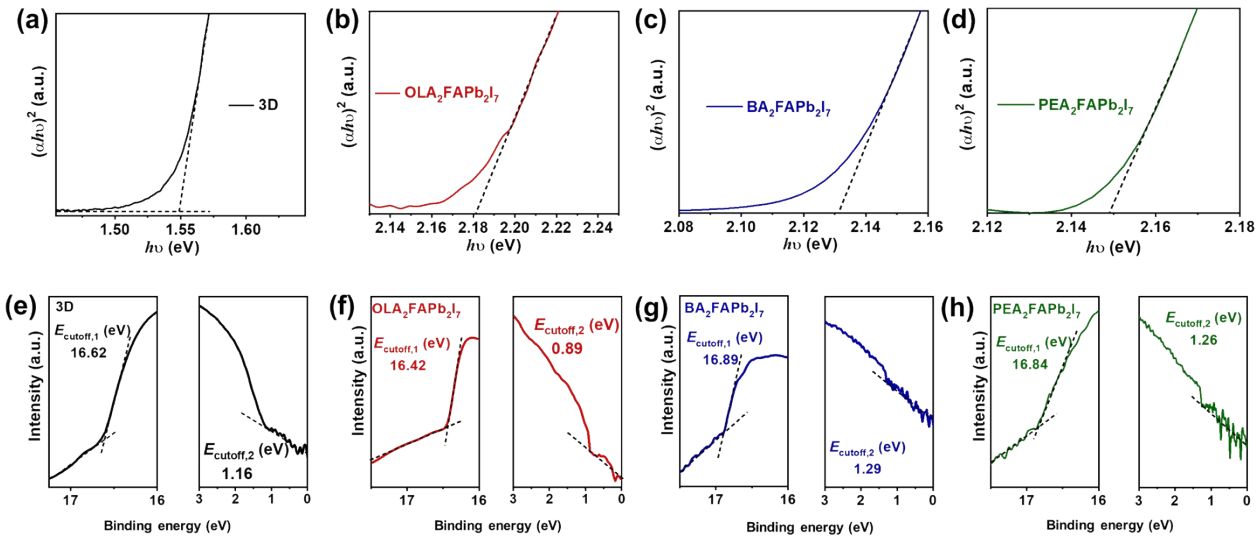

Fig. S4 Tauc plots of a) 3D and b) $OLA_2Pb_2I_7$, c) $BA_2FAPb_2I_7$, and d) $PEA_2FAPb_2I_7$ 2D perovskite. Magnified regions of UPS spectra of large binding energy ($E_{cutoff,1}$) and low binding energy ($E_{cutoff,2}$) for e) 3D, and f) $OLA_2Pb_2I_7$, g) $BA_2FAPb_2I_7$ and h) $PEA_2FAPb_2I_7$ 2D perovskite. Note: the Y-axis in the figures used the logarithmic scale, which can avoid the overestimation of the valence band edge.

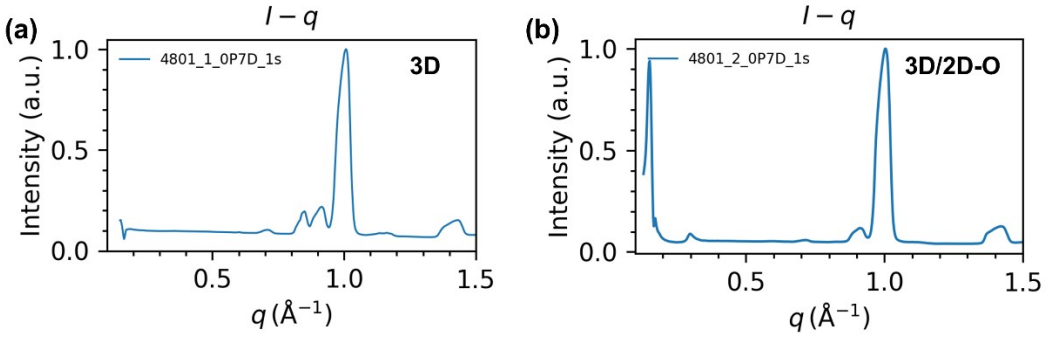

Fig. S5 Integrated intensity of GIWAXS data along q_z of (a) 3D perovskite and (b) 3D/2D-O perovskite films.

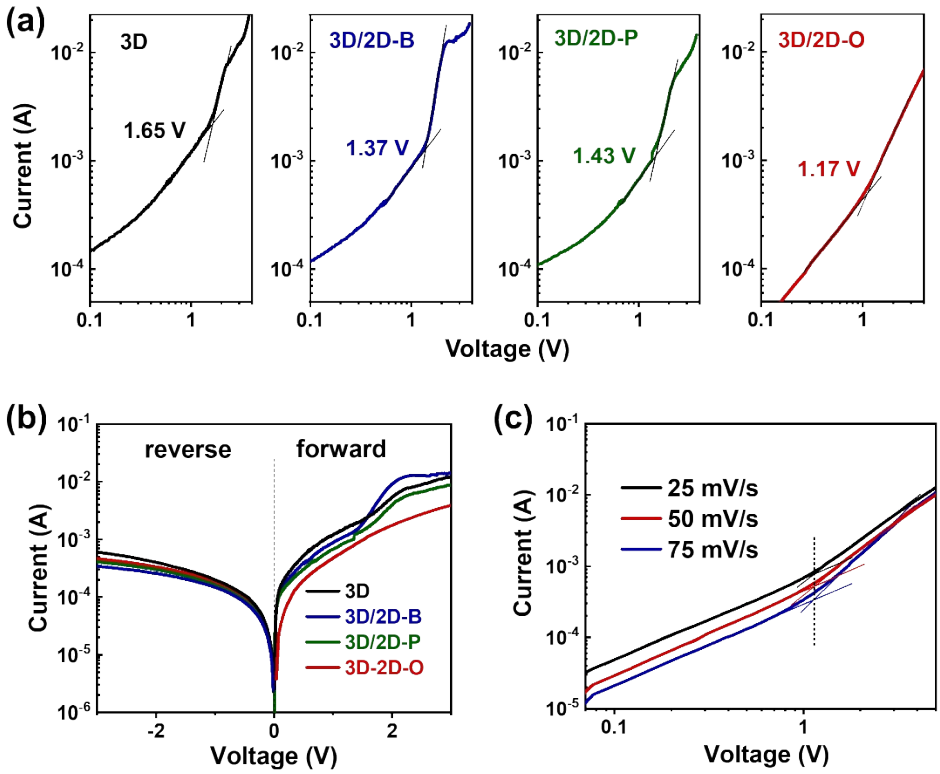

Fig. S6 (a) The dark *J*–*V* curves and V_{TFL} determination of electron-only devices. (b) *J*–*V* curves of electron-only devices in both positive and negative directions. (c) *J*–*V* curves of 3D-O device measured at different scan rates.

Note: The density of defect states can be calculated using the following equation:

$$N_{(t)} = \frac{2\varepsilon_r \varepsilon_0 V_{TFL}}{qL^2}$$

where ε_r is the relative permittivity, ε_0 is the vacuum permittivity, V_{TFL} is the onset voltage of the trap-filled limit, q is the elementary charge, and L is the thickness of the perovskite film.

We also measured the *J*–*V* curves of the electron-only devices in both positive and negative directions. As shown in Fig. S6b, both the positive and negative scans showed increased current with the increase of voltage, confirming the electron can be successfully injected and the absence of an injection barrier. The *J*–*V* curves with different scan rates are shown in Fig. S6c. It can be found that the scan rate has negligible influence on the determination of V_{TFL}.

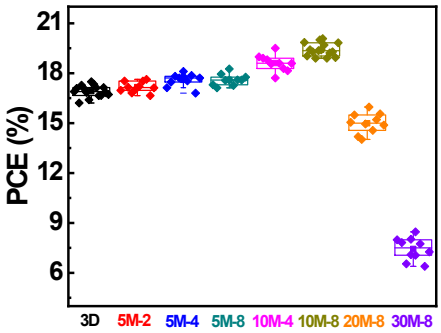

Fig. S7 Summarization and distribution of photovoltaic parameters at various concentrations and droplet number of OLAI solution. For the expression, the optimized condition of '10M-8' represents the application of 10 mg/mL of OLAI precursor solution, and 8 drops of solution were dipped onto the film during dynamic spin-coating.

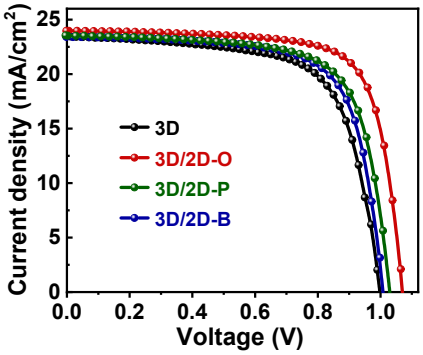

Fig. S8 *J–V* curves (forward scan) of the devices based on 3D and 3D/2D perovskite films.

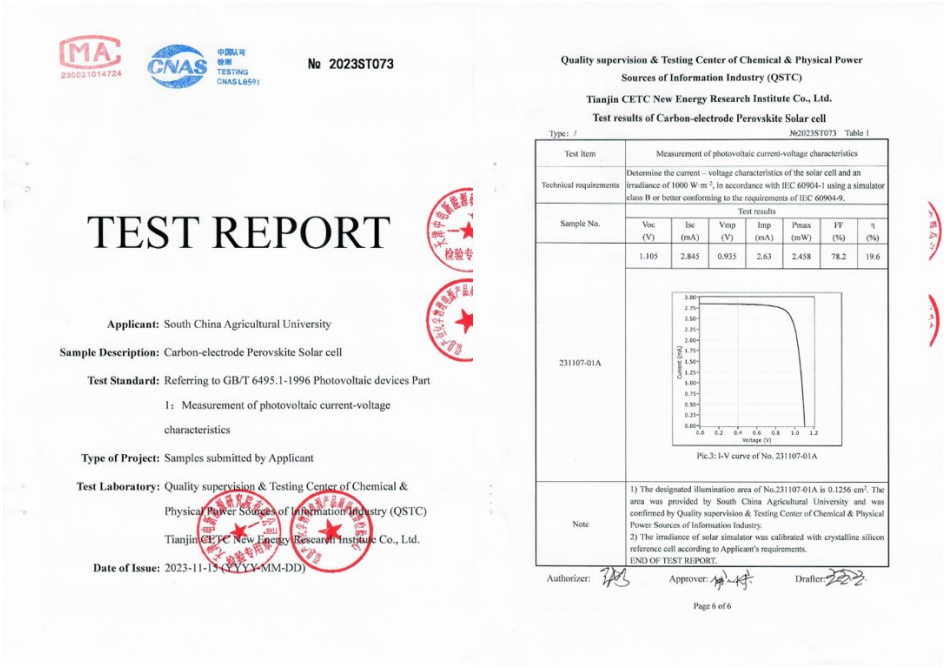

No 2023ST073

TEST REPORT

Applicant: South China Agricultural University

Sample Description: Carbon-electrode Perovskite Solar cell

Test Standard: Referring to GB/T 6495.1-1996 Photovoltaic devices Part 1: Measurement of photovoltaic current-voltage characteristics

Type of Project: Samples submitted by Applicant

Test Laboratory: Quality supervision & Testing Center of Chemical & Physical Power Sources of Information Industry (QSTC) Tianjin CETC New Energy Research Institute Co., Ltd.

Date of Issue: 2023-11-15 (YYYY-MM-DD)

Quality supervision & Testing Center of Chemical & Physical Power Sources of Information Industry (QSTC)

Tianjin CETC New Energy Research Institute Co., Ltd.

Test results of Carbon-electrode Perovskite Solar cell

Type: / №2023ST073 Table 1

Test Item	Measurement of photovoltaic current-voltage characteristics						
Technical requirements	Determine the current – voltage characteristics of the solar cell and an irradiance of 1000 W·m^{-2}, in accordance with IEC 60904-1 using a simulator class B or better conforming to the requirements of IEC 60904-9.						
Sample No.	Test results						
	Voc (V)	Isc (mA)	Vmp (V)	Imp (mA)	Pmax (mW)	FF (%)	η (%)
231107-01A	1.105	2.845	0.935	2.63	2.458	78.2	19.6

Pic.3: I-V curve of No. 231107-01A

Note	1) The designated illumination area of No.231107-01A is 0.1256 cm^2. The area was provided by South China Agricultural University and was confirmed by Quality supervision & Testing Center of Chemical & Physical Power Sources of Information Industry. 2) The irradiance of solar simulator was calibrated with crystalline silicon reference cell according to Applicant's requirements. END OF TEST REPORT.

Authorizer: Approver: Drafter:

Page 6 of 6

Fig. S9 Certified results of one device by QSTC (Quality supervision & Testing Center of Chemical & Physical Power Sources of Information Industry, China).

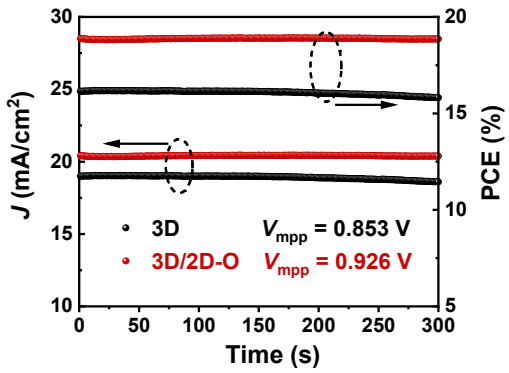

Fig. S10 Stabilized power output (SPO) curves of 3D and 3D/2D-O devices.

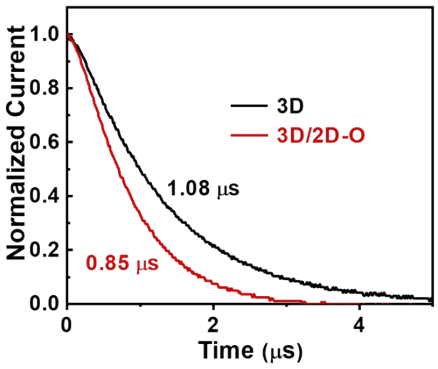

Fig. S11 Transient photocurrent decay (TPC) curves of 3D and 3D/2D-O devices.

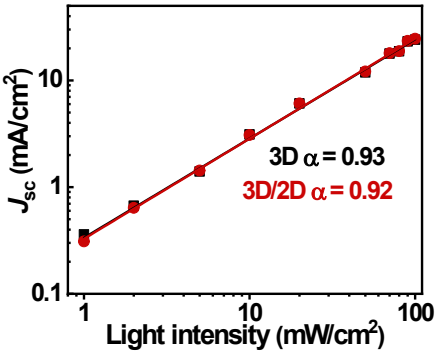

Fig. S12 Light intensity-dependent J_{sc} curves of 3D and 3D/2D-O perovskite-based devices.

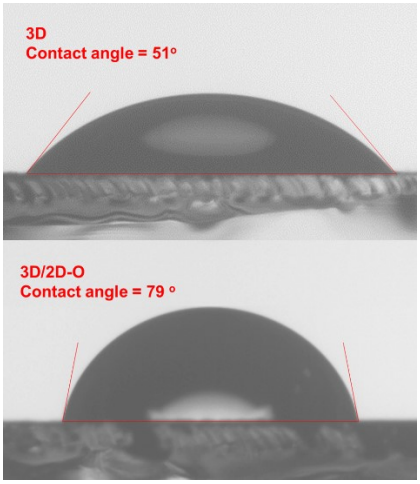

Fig. S13 Water contact angle of 3D and 3D/2D-O perovskite films.

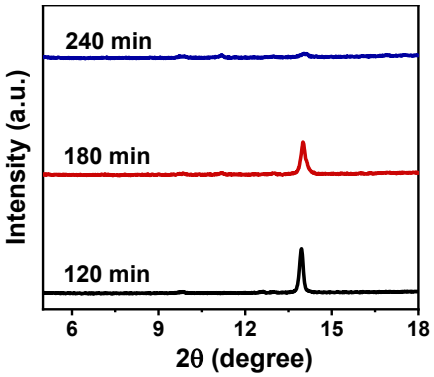

Fig. S14 XRD pattern evolution of 3D/2D-O perovskite films soaking in water for more than 120 min.

Table S1 Hall effect measurements of different 2D perovskite films.

Sample	Carrier density (cm^{-3})	Hall coefficient (cm^3/c)	Type
2D-O	1.91×10^{20}	0.033	p
2D-B	6.56×10^{19}	-0.095	n
2D-P	2.83×10^{20}	-0.021	n

Table S2 Fitting parameters of 3D and 3D/2D perovskite films.

Sample	A_1	τ_1 (ns)	A_2	τ_2 (ns)	τ (ns)
3D	315.17	13.66	602.32	162.56	156.29
3D/2D-O	352.77	22.77	611.89	111.66	102.31
3D/2D-P	262.68	22.52	683.30	198.70	191.34
3D/2D-B	271.84	24.64	675.09	218.78	210.36

Table S3 Photovoltaic parameters of PSCs at various concentrations (mg/mL) and droplet number of OLAI solution.

Conc/droplet	V_{oc} [V]	J_{sc} [mA cm^{-2}]	FF [%]	PCE [%]
5/2	1.02 ± 0.01 (1.03)	23.29 ± 0.27 (23.72)	71.98 ± 0.82 (71.81)	17.16 ± 0.25 (17.53)
5/4	1.04 ± 0.01 (1.04)	23.35 ± 0.29 (23.46)	72.66 ± 0.67 (74.23)	17.59 ± 0.29 (18.11)
5/8	1.04 ± 0.01 (1.06)	23.37 ± 0.28 (23.40)	72.85 ± 0.59 (74.03)	17.60 ± 0.23 (18.26)
10/4	1.05 ± 0.01 (1.07)	23.53 ± 0.28 (23.93)	75.12 ± 0.52 (75.80)	18.61 ± 0.35 (19.50)
10/8 (target)	1.07 ± 0.01 (1.09)	23.86 ± 0.23 (24.04)	75.95 ± 0.76 (76.98)	19.41 ± 0.31 (20.08)
20/8	1.01 ± 0.02 (1.05)	23.19 ± 0.42 (23.06)	64.05 ± 2.30 (66.08)	14.98 ± 0.47 (15.97)
30/8	0.97 ± 0.03 (0.92)	16.22 ± 0.70 (16.38)	47.40 ± 3.82 (56.13)	7.44 ± 0.57 (8.46)

Table S4 Photovoltaic parameters of C-PSCs based on 3D and 3D/2D perovskite films and the calculated S-Q limit parameters of PSC with a band gap of 1.55 eV. (R represents reverse scan, F represents forward scan)

Device		V_{oc} [V]	J_{sc} [mA cm^{-2}]	FF [%]	PCE [%]
S-Q limits		1.28	27.27	90.25	31.44
	average	1.02 ± 0.01	23.25 ± 0.25	71.43 ± 1.07	16.92 ± 0.28
3D	champion (R)	1.04	23.58	71.38	17.49
	champion (F)	1.00	23.45	67.69	15.59
	average	1.07 ± 0.01	23.86 ± 0.23	75.95 ± 0.76	19.41 ± 0.31
3D/2D-O	champion (R)	1.09	24.04	76.98	20.08
	champion (F)	1.07	23.97	74.11	19.04
	average	1.03 ± 0.01	23.37 ± 0.31	71.69 ± 1.46	17.18 ± 0.52
3D/2D-B	champion (R)	1.04	23.54	73.66	18.08
	champion (F)	1.01	23.40	70.67	16.68
	average	1.05 ± 0.01	23.35 ± 0.20	72.53 ± 1.57	17.74 ± 0.44
3D/2D-P	champion (R)	1.06	23.60	74.00	18.46
	champion (F)	1.03	23.52	71.03	17.22

Table S5 Summary of the representative photovoltaic performance of the planar HTL-free carbon electrode-based PSCs (> 16%)

Perovskite	Device structure	J_{sc} [mA cm^{-2}]	V_{oc} [V]	FF	PCE [%]	Ref.
$FA_{0.83}Cs_{0.17}PbI_3$	FTO/SnO_2/PVK/C	24.04	1.09	0.769	20.08	This work
$FAPbI_3$	FTO/c-TiO_2/m-TiO_2/PVK/C	24.30	1.03	0.739	18.50	[13]
$FA_{0.6}Cs_{0.4}PbI_3$	FTO/c-TiO_2/m-TiO_2/PVK/C	22.95	1.00	0.781	17.69	[14]
$FA_{0.6}Cs_{0.4}PbI_3$	FTO/c-TiO_2/m-TiO_2/PVK/C	22.90	1.01	0.782	18.08	[15]
$FA_{0.6}Cs_{0.4}PbI_3$	FTO/c-TiO_2/m-TiO_2/PVK/C	23.48	1.03	0.789	19.06	[16]
$FA_{0.6}Cs_{0.4}PbI_3$	FTO/c-TiO_2/m-TiO_2/PVK/C	22.82	1.03	0.788	18.52	[17]
$CsPbI_3$	FTO/c-TiO_2/PVK/C	20.13	1.11	0.808	18.05	[18]
$Cs_{0.5}FA_{0.5}PbI_3$	FTO/c-TiO_2/m-TiO_2/PVK/C	21.53	0.97	0.777	16.30	[19]
$MAPbI_3$	FTO/c-TiO_2/m-TiO_2/PVK/C	23.84	0.97	0.708	16.40	[20]
$GA_{0.2}MA_{0.8}PbI_3$	FTO/SnO_2/PVK/C	22.74	1.10	0.646	16.19	[21]
$MAPbI_3$	ITO/SnO_2/PVK/C	19.90	1.14	0.726	16.45	[22]
$MAPbI_3$	FTO/SnO_2/PVK/C	23.85	1.10	0.718	18.90	[23]
$Cs_{0.05}MA_{0.95}PbI_3$	ITO/C_{60}/PVK/C	22.72	1.12	0.730	18.64	[24]
$FA_{0.9}MA_{0.1}PbI_3$	FTO/SnO_2/PVK/C	24.66	1.09	0.721	19.41	[25]
$FA_{0.9}MA_{0.1}PbI_3$	FTO/SnO_2/PVK/C	23.66	1.11	0.743	19.42	[26]
$CsPbI_3$	FTO/TiO_2/PVK/C	19.84	1.13	0.823	18.47	[27]
$MAPbI_3$	ITO/SnO_2/PVK/C	23.42	1.07	0.72	18.13	[28]
$MAPbI_3$	FTO/TiO_2/PVK/PQD/C	22.52	1.06	0.751	17.93	[29]
$FA_xMA_{1-x}PbI_3$	ITO/SnO_2/PVK/C	23.18	1.06	0.711	17.49	[30]
$MAPbI_3$	ITO/SnO_2/PVK/C	23.63	1.11	0.651	17.06	[31]
$MAPbI_3$	ITO/SnO_2/PVK/C	22.78	1.16	0.65	17.27	[32]
$FA_{0.6}Cs_{0.4}PbI_3$	FTO/c-TiO_2/m-TiO_2/PVK/C	23.50	1.05	0.791	19.52	[33]

Table S6 Efficiency loss results of 3D and 3D/2D-O based C-PSCs.

Sample	$V_{oc}^{real}/V_{oc}^{SQ}$	J_{sc}/J_{sc}^{SQ}	$FF^{real}/FF_0(V_{oc}^{SQ})$	$V_{oc}^{real}/V_{oc}^{rad}$	V_{oc}^{rad}/V_{oc}^{SQ}	$FF_0(V_{oc}^{real})/FF_0(V_{oc}^{SQ})$	$FF^{real}/FF_0(V_{oc}^{real})$	PCE/PCE^{SQ}
3D	79.81%	85.25%	79.15%	87.46%	91.25%	97.94%	80.80%	53.81%
3D/2D-O	83.72%	87.50%	84.16%	89.24%	93.82%	98.40%	85.51%	61.72%

Table S7 EIS parameters of 3D and 3D/2D-O based devices.

Device	R_s (Ω cm^2)	C_μ (mF cm^{-2})	R_{rec} (Ω cm^2)
3D	67.39	3.09×10^{-8}	101.5
3D/2D-O	63.53	4.76×10^{-8}	250.2

References

1. R. M. Maceiczyk, K. Dumbgen, I. Lignos, L. Protesescu, M. V. Kovalenko and A. J. deMello, *Chem. Mater.*, 2017, **29**, 8433–8439.
2. T. Bu, J. Li, H. Li, C. Tian, J. Su, G. Tong, L. K. Ono, C. Wang, Z. Lin, N. Chai, X.-L. Zhang, J. Chang, J. Lu, J. Zhong, W. Huang, Y. Qi, Y.-B. Cheng and F. Huang, *Science*, 2021, **372**, 1327–1332.
3. H. Chen, S. Teale, B. Chen, Y. Hou, L. Grater, T. Zhu, K. Bertens, S. M. Park, H. R. Atapattu, Y. J. Gao, M. Y. Wei, A. K. Johnston, Q. L. Zhou, K. M. Xu, D. N. Yu, C. C. Han, T. Cui, E. H. Jung, C. Zhou, W. J. Zhou, A. H. Proppe, S. Hoogland, F. Laquai, T. Filleter, K. R. Graham, Z. J. Ning and E. H. Sargent, *Nat. Photonics*, 2022, **16**, 352.
4. D. Xu, R. Mai, Y. Jiang, C. Chen, R. Wang, Z. Xu, K. Kempa, G. Zhou, J. Liu and J. Gao, *Energy Environ. Sci.*, 2022, **15**, 3891–3900.
5. J. Endres, D. A. Egger, M. Kulbak, R. A. Kerner, L. Zhao, S. H. Silver, G. Hodes, B. P. Rand, D. Cahen, L. Kronik and A. Kahn, *J. Phys. Chem. Lett.*, 2016, **7**, 2722–2729.

6. B. Yang, J. Suo, F. Di Giacomo, S. Olthof, D. Bogachuk, Y. Kim, X. Sun, L. Wagner, F. Fu, S. M. Zakeeruddin, A. Hinsch, M. Grätzel, A. Di Carlo and A. Hagfeldt, *ACS Energy Lett.*, 2021, **6**, 3916–3923.
7. Y. Yuan, G. Yan, R. Hong, Z. Liang and T. Kirchartz, *Adv. Mater.*, 2022, **34**, 2108132.
8. H. Xu, Z. Liang, J. Ye, Y. Zhang, Z. Wang, H. Zhang, C. Wan, G. Xu, J. Zeng, B. Xu, Z. Xiao, T. Kirchartz and X. Pan, *Energy Environ. Sci.*, 2023, **16**, 5792–5804.
9. J.-F. Guillemoles, T. Kirchartz, D. Cahen and U. Rau, *Nat. Photonics*, 2019, **13**, 501–505.
10. G. Kresse and D. Joubert, *Phys. Rev. B*, 1999, **59**, 1758–1775.
11. J. P. Perdew, K. Burke and M. Ernzerhof, *Phys. Rev. Lett.*, 1996, **77**, 3865–3868.
12. J. Heyd and G. E. Scuseria, *J. Chem. Phys.*, 2004, **121**, 1187–1192.
13. S. Zouhair, S. M. Yoo, D. Bogachuk, J. P. Herterich, J. Lim, H. Kanda, B. Son, H. J. Yun, U. Würfel, A. Chahboun, M. K. Nazeeruddin, A. Hinsch, L. Wagner and H. Kim, *Adv. Energy Mater.*, 2022, **12**, 2200837.
14. L. Li, R. Zhang, Z. Wu, Y. Wang, J. Hong, H. Rao, Z. Pan and X. Zhong, *Chem. Eng. J.*, 2023, **455**, 140566.
15. Z. Wu, Y. Wang, L. Li, R. Zhang, J. Hong, R. Huang, L. Che, G. Yang, H. Rao, Z. Pan and X. Zhong, *Small*, 2023, **19**, e2300690.
16. Y. Wang, L. Li, Z. Wu, R. Zhang, J. Hong, J. Zhang, H. Rao, Z. Pan and X. Zhong, *Angew. Chem. Int. Ed.*, 2023, **62**, e202302342.
17. R. Zhang, L. Li, W. Wang, Z. Wu, Y. Wang, J. Hong, H. Rao, Z. Pan and X. Zhong, *Adv. Funct. Mater.*, 2023, **33**, 2300552.
18. J. Zhang, G. Zhang, P. Y. Su, R. Huang, J. Lin, W. Wang, Z. Pan, H. Rao and X. Zhong, *Angew. Chem. Int. Ed.*, 2023, **62**, e202303486.
19. Z. Huang, L. Li, H. Rao, Z. Pan and X. Zhong, *Sol. RRL*, 2022, **6**, 2200145.
20. T. Liu, Y. Li, R. Xu, L. Lou, J. Gao, K. Zhang, M. Su, W. Qian, G. Wang, S. Xiao and S. Yang, *Sol. RRL*, 2022, **6**, 2200206.
21. Y. Li, S. Li, Y. Li, X. Sun, X. D. Lv, Y. Zheng, M. Huang and X. Tao, *Sol. RRL*, 2022, **6**, 2101103.
22. Y. Cheng, Q. Wei, Z. Ye, X. Zhang, P. Ji, N. Wang, L. Zan, F. Fu and S. Liu, *Sol. RRL*, 2022, **6**, 2200418.
23. T. Ye, Y. Hou, A. Nozariasbmarz, D. Yang, J. Yoon, L. Zheng, K. Wang, K. Wang, S. Ramakrishna and S. Priya, *ACS Energy Lett.*, 2021, **6**, 3044–3052.
24. T. Tian, J. Zhong, M. Yang, W. Feng, C. Zhang, W. Zhang, Y. Abdi, L. Wang, B. Lei and W. Wu, *Angew. Chem. Int. Ed.*, 2021, **60**, 23735–23742.

25. J. Ma, S. Lin, M. Fang, Z. Fang, X. Yu, D. E. Guo, H. Xie, D. Kong, Y. Li and C. Zhou, *Small*, 2024, 2310196.
26. S. Lin, Z. Fang, J. Ma, D. e. Guo, X. Yu, H. Xie, M. Fang, D. Zhang, K. Zhou, Y. Gao and C. Zhou, *Small Methods*, 2023, **8**, 2300716.
27. W. Wang, X. Peng, J. Zhang, J. Lin, R. Huang, G. Zhang, H. Guo, Z. Pan, X. Zhong and H. Rao, *J. Energy Chem.*, 2024, **93**, 221–228.
28. D. Wu, H. Zhou, X. Lai, X. Liu, K. Sang, Y. Chen, M. Chen, J. Wei, S. Wu, Q. Pang, L. Zhou and P. Chen, *Small*, 2023, 2308783.
29. Y. Yang, S. Wang, S. Li, T. Li, P. Chen, Q. Zhao and G. Li, *Sol. RRL*, 2023, **7**, 2300606.
30. S. Li, Y. Li, X. Sun, Y. Li, F. Deng and X. Tao, *Chem. Eng. J.*, 2023, **455**, 140727.
31. Q. Wei, N. Wang, Y. Gao, Y. Zhuansun, J. Wang, D. Zhu, L. Zan, F. Fu and Y. Liu, *ACS Appl. Mater. Interfaces*, 2024, **16**, 20803–20812.
32. Q. Wei, Z. Ye, Y. Gao, N. Wang, L. Feng, Q. Zhao, X. Hou, L. Zan, F. Fu and D. Yang, *J. Mater. Chem. A*, 2024, **12**, 1573–1581.
33. L. Li, H. Rao, Z. Wu, J. Hong, J. Zhang, Z. Pan and X. Zhong, *Adv. Funct, Mater.*, 2024, **34**, 2308428.